

Carbon and sulfur budget of the silicate Earth explained by accretion of differentiated planetary embryos

Yuan Li^{1*}, Rajdeep Dasgupta¹, Kyusei Tsuno¹, Brian Monteleone², and Nobumichi Shimizu².

1. Department of Earth Science, Rice University, 6100 Main Street, MS 126, Houston, TX 77005.

2. Department of Geology and Geophysics, Woods Hole Oceanographic Institution, Woods Hole, MA 02543.

Supplementary Material

Calculating carbon abundance and C/S ratio of Earth's mantle during accretion

The carbon abundance retained in Earth's mantle during accretion was calculated using Eqs.3-4 (see Methods), in the framework of continuous core formation model^{1,2}, following the method of Boujibar et al³. In this method, four models for the variation of fO_2 during accretion was used and tested (Supplementary Fig. 9a), and in each accretion stage (100 stages in total) the equilibrium pressure is equivalent to the pressure of half of the depth of the mantle and the equilibrium temperature was assumed to be liquidus of the mantle. The liquidus determined for pyrolite at <25 GPa and the liquidus determined for a chondrite at >25 GPa were taken as mantle liquidus³⁻⁵.

Supplementary Figure 9b shows the calculated $D_C^{alloy/silicate}$ during accretion, at conditions corresponding to models a-d in Supplementary Figure 9a. In models a-b, that

*Present Address: Guangzhou Institute of Geochemistry, Chinese Academy of Sciences, Guangzhou, 510640, China.

capture two relatively reduced paths of terrestrial accretion, Eq. 4 was used, and in models c-d, where initial conditions were more oxidized, Eq. 3 was used. The Ni and S contents in the alloy were fixed to be 5 wt.% and 1.2 wt.%, respectively. The Si content in the alloy was varied from 10 to 0 wt.% from low fO_2 to high fO_2 in models a-b, according to the correlation of fO_2 and Si content in alloy observed in this study and the study of Boujibar et al³. The melt water content was fixed to be 0.3 wt.%, which was estimated to be the water content of the bulk Earth⁶. Considering the high volatility of carbon during accretion, the bulk Earth carbon abundance was chosen to be 1000 and 5000 p.p.m, which are well comparable to the bulk Earth sulfur abundance of 6500 p.p.m chosen by Boujibar et al³. These values chosen were conservative, because carbon is more volatile than sulfur and the carbon abundance in all kinds of chondrites is indeed much lower than the sulfur abundance (Supplementary Fig. 1).

The calculated carbon abundance in Earth's mantle during accretion was presented in Supplementary Figure 9c, d. These calculated values (0.6-3.3 p.p.m) are significantly lower than the carbon abundance estimated for the Earth's present mantle (35-115 p.p.m)⁷, and are also significantly lower than the sulfur abundance (150-250 p.p.m) estimated for the Earth's present mantle^{8,9} and the sulfur abundance (200-500 p.p.m) calculated by Boujibar et al³ for the Earth's mantle during accretion. Therefore, the Earth's present mantle C/S ratio cannot be established during Earth's continuous accretion (Supplementary Fig. 10).

To illustrate further that the C/S ratio in Earth's mantle established during accretion is significantly lower than the Earth's present mantle C/S ratio, the C/S ratio resulting from a single stage, equilibrium core formation model was also calculated (Supplementary Fig. 10). In this model, considering the fact that fO_2 is the main factor controlling $D_C^{alloy/silicate}$ and $D_S^{alloy/silicate}$ and in order to avoid large uncertainties in the application of the experimental data to a deep MO by extrapolation, three pairs of $D_C^{alloy/silicate}$ and $D_S^{alloy/silicate}$ obtained directly from high-pressure experiments (Fig. 1), corresponding to MOs with different oxygen fugacities, were chosen. This has been done similarly for modelling the fractionation of light elements C, N, and H in MOs by previous studies¹⁰⁻¹³. The calculated results (Supplementary Fig. 10) show that the mantle C/S ratio obtained in a single stage core formation model is also

significantly lower than the Earth's present mantle C/S ratio. Therefore, in any physically realistic model of Earth's accretion, the Earth's present mantle C/S ratio could not have been established if carbon and sulfur were delivered simultaneously to Earth's MO in a chondritic ratio and if equilibrium core formation occurs in the terrestrial MO.

Calculating $D_C^{sulfide/silicate}$

The partition coefficients of carbon between sulfide and silicate melt ($D_C^{sulfide/silicate}$) were calculated based on the experimentally measured carbon solubility in sulfide (Fig. 1b) and the calculated carbon solubility in a peridotitic melt at the Fe-FeO buffer and at the corresponding P - T conditions. The carbon solubility in a peridotitic melt was calculated using the parameterization of all the experimental data presented in Supplementary Figure 4, between $\log f_{O_2}$ IW-1.5 and IW and pressure and temperature of 1-6 GPa and 1345-2000 °C:

$$\log(C, \text{ppm}) = -3362/T - 110P/T + 0.86X_{H_2O} + 0.66NBO/T + 0.26\Delta IW + 2.9 \quad (R^2 = 0.72) \quad (1)$$

in which T is temperature in K, P is pressure in GPa, X_{H_2O} is mole fraction of water in silicate melt, and ΔIW is the oxygen fugacity relative to the Fe-FeO buffer. The calculated $D_C^{sulfide/silicate}$ is between 10 and 500 when sulfur in the sulfide is between 25 and 40 wt.%.

Supplementary Figures and Tables

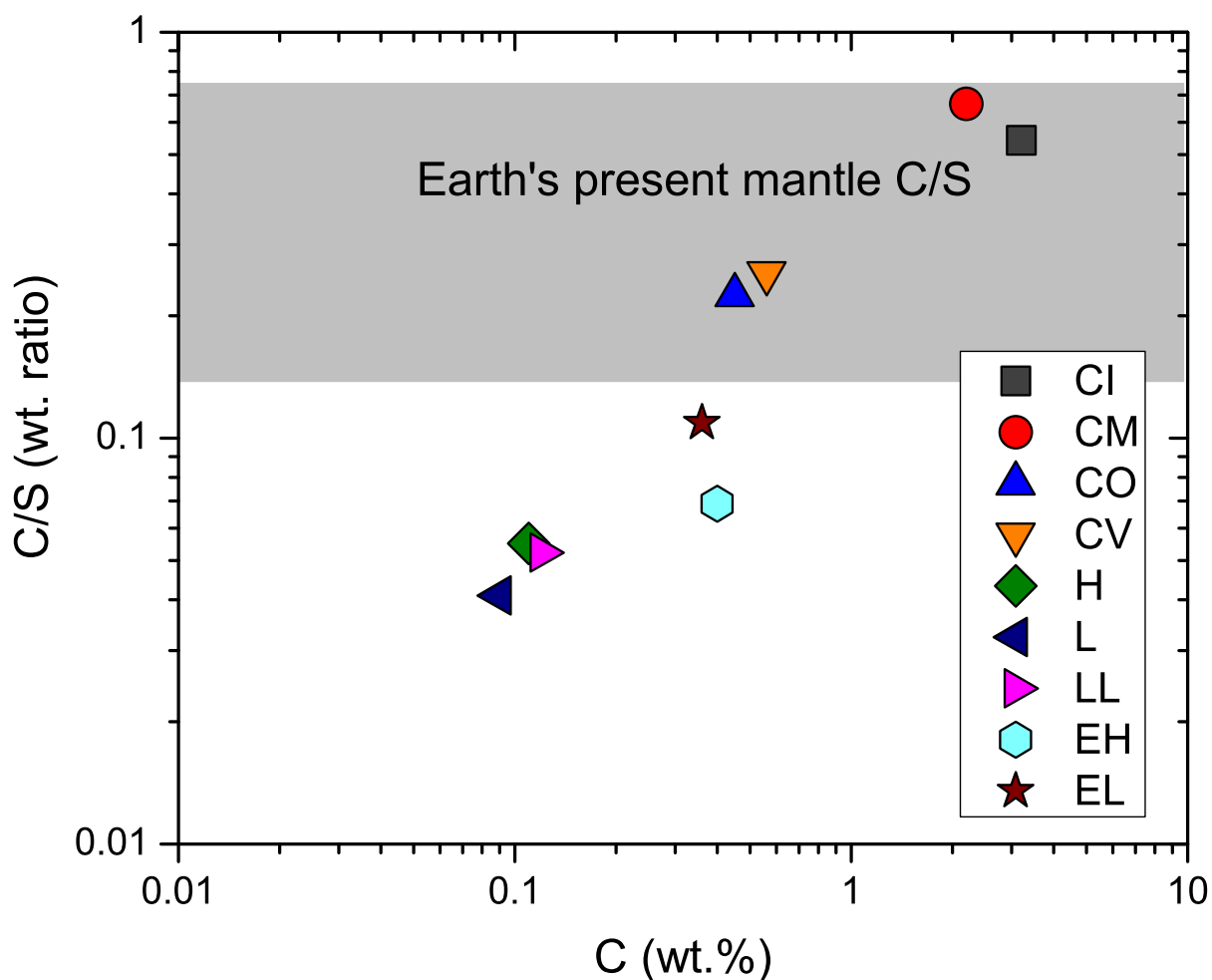


Figure S1. The carbon content and C/S ratio of different chondrites. The data were taken from ref. 14. The Earth's present mantle C/S ratio was calculated using 150-250 p.p.m S and 35-115 p.p.m carbon estimated for the bulk silicate mantle⁷⁻⁹. Note that the Earth's present mantle C/S ratio is similar to that of carbonaceous chondrites.

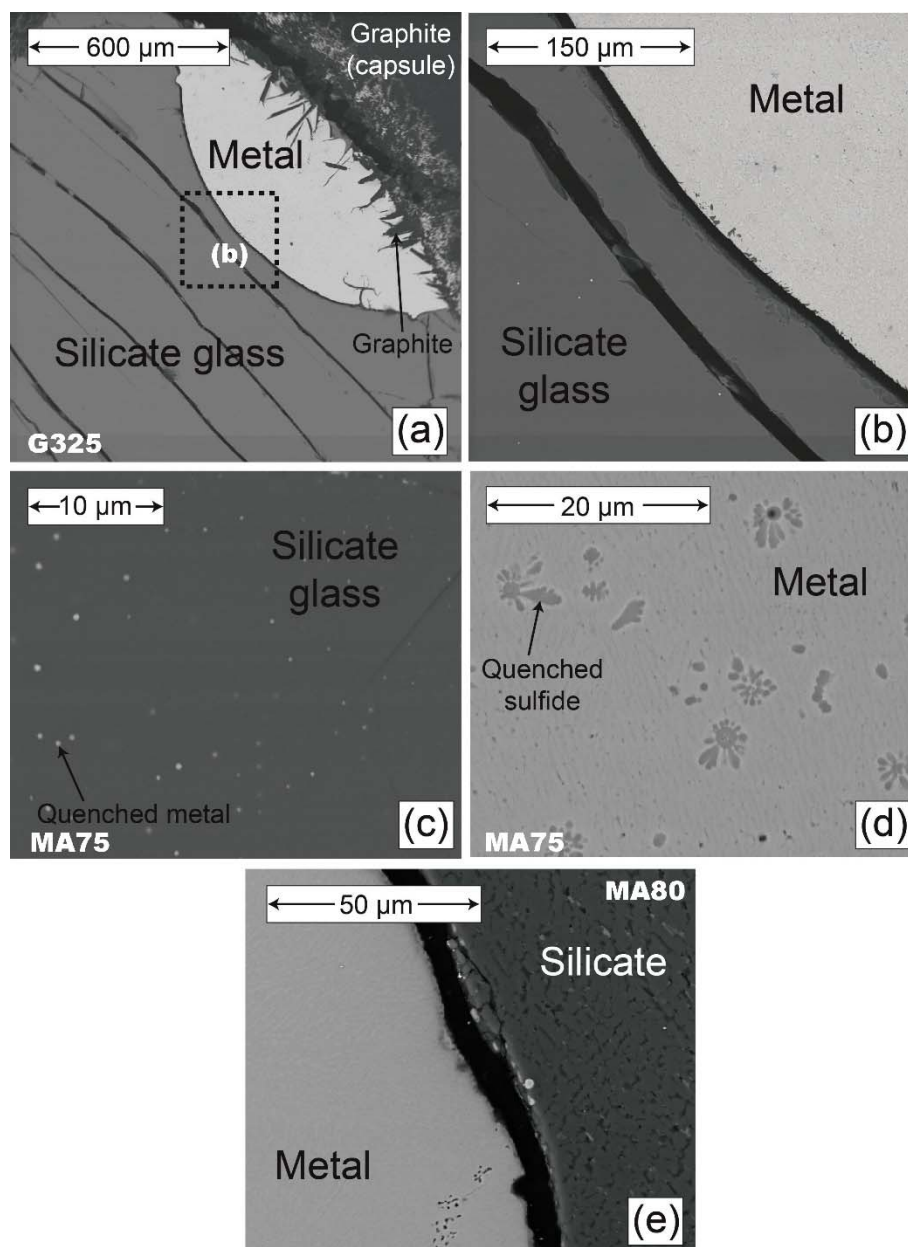


Figure S2. Selected back-scattered electron images of run products. **a**, Coexistence of quenched silicate melt and alloy melt from run G325. **b**, Detailed texture of quenched silicate melt and alloy melt in (a). **c**, **d**, Detailed texture of quenched silicate melt and alloy melt from run MA75. **e**, Texture of coexisting quenched alloy melt and silicate melt from run MA80. Note that in this run typical quench crystals were produced from the silicate melt during quench.

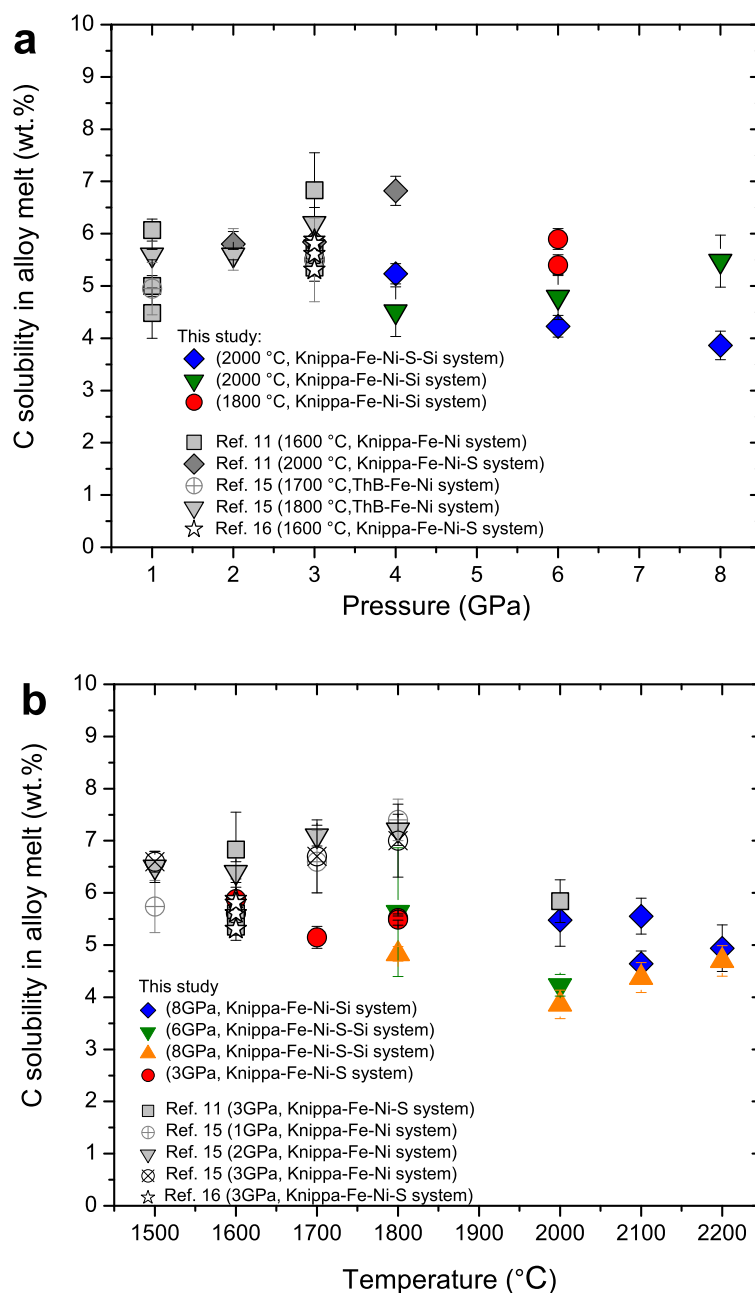


Figure S3. The carbon solubility in alloy melt as a function of pressure and temperature.

In a given system, the carbon solubility in alloy melt is almost constant within analytical error, independent of pressure or temperature. The observed small variation is mainly caused by the variation of S and/or Si contents in the alloy melt (see Fig. 1).

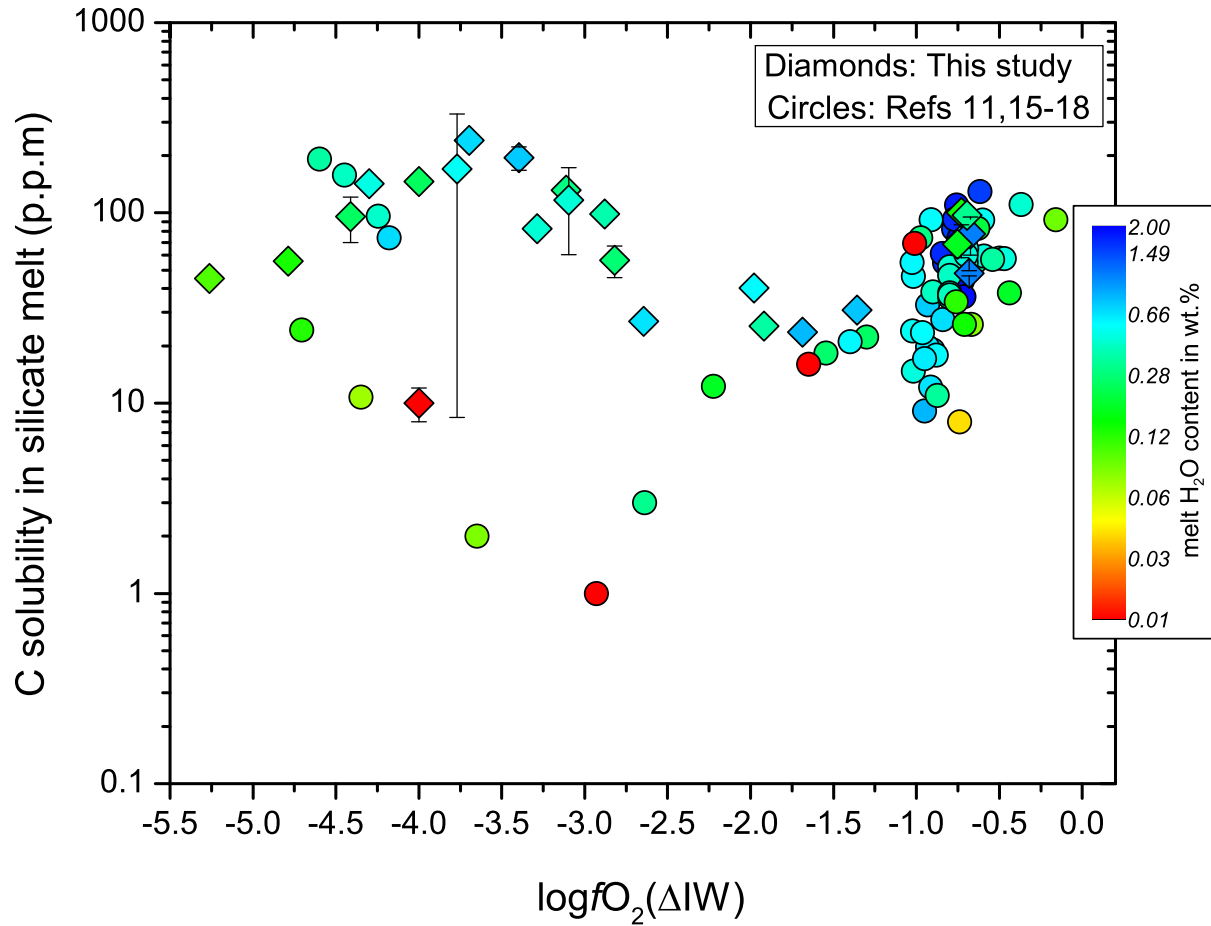


Figure S4. The carbon solubility in silicate melt at graphite saturation as a function of oxygen fugacity and melt H₂O content. Note that the solution behavior of carbon changes at the oxygen fugacity of $\leq \Delta IW - 1.5$, depending on the bulk water content. This possible change is mainly due to the potential change of carbon species in silicate melt as function of oxygen fugacity and melt water content. See text for more details.

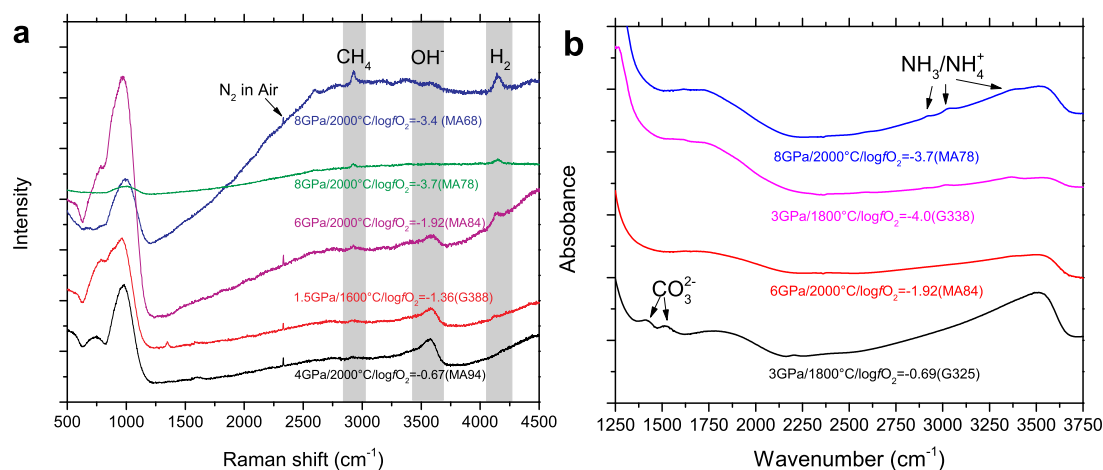


Figure S5. Typical Raman and FTIR spectra of silicate glasses from this study showing regions associated with C-H-O volatile species. a, In the Raman spectra, the peak intensity of water generally decreases with decreasing oxygen fugacity, while the peak intensities of CH_4 and H_2 increase. **b,** In the FTIR spectra, the peaks of CO_3^{2-} doublets are only resolvable at oxidized conditions, while at reduced conditions they disappear but some N-H peaks appear. All the oxygen fugacity values are relative to the Fe-FeO (IW) buffer following the non-ideal solution model for alloy and silicate melt (see Supplementary Table 1).

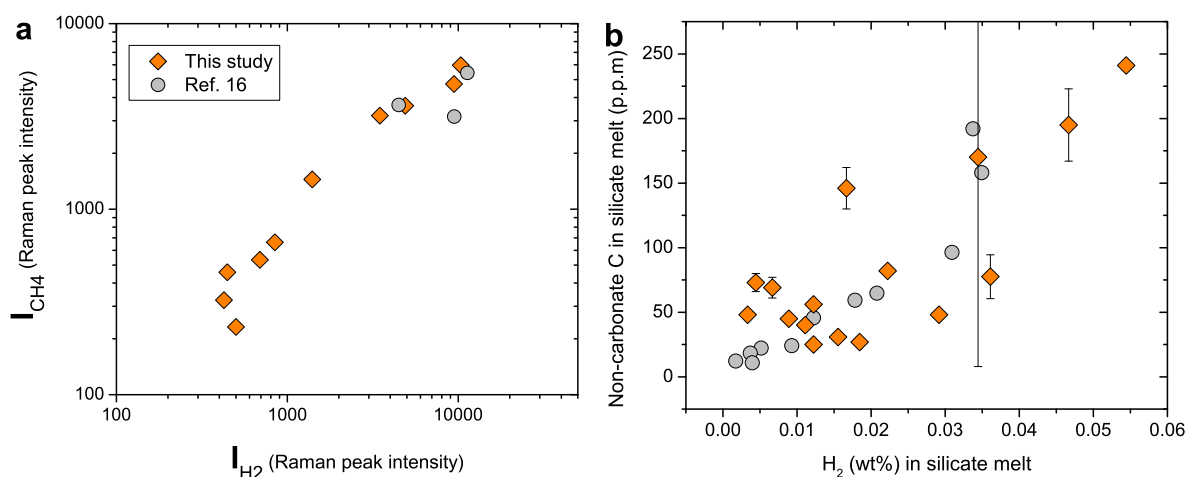


Figure S6. The correlations between Raman peak intensities of molecular H_2 and CH_4 in silicate melt (a) and between non-carbonate carbon and molecular H_2 contents in silicate melt (b). These strong correlations indicate that carbon in the silicate melt is mainly as hydrogenated carbon species (e.g., CH_4). Note that molecular H_2 in panel (b) refers to all the non-hydroxyl hydrogen in silicate melt and equals the bulk hydrogen determined using SIMS minus the hydrogen in the form of hydroxyl determined using FTIR using the Beer-Lambert law. In panel (b) for simplification, only the hydroxyl hydrogen contents determined at $\epsilon_{\text{OH}^-} = 60 \text{ L mol}^{-1}\text{cm}^{-1}$ were used; the strong correlation would not change at all if $\epsilon_{\text{OH}^-} = 90 \text{ L mol}^{-1}\text{cm}^{-1}$ is used. The non-carbonate carbon and the bulk carbon measured using SIMS are the same for all the experiments with $\log f\text{O}_2 < \text{IW}-1.3$.

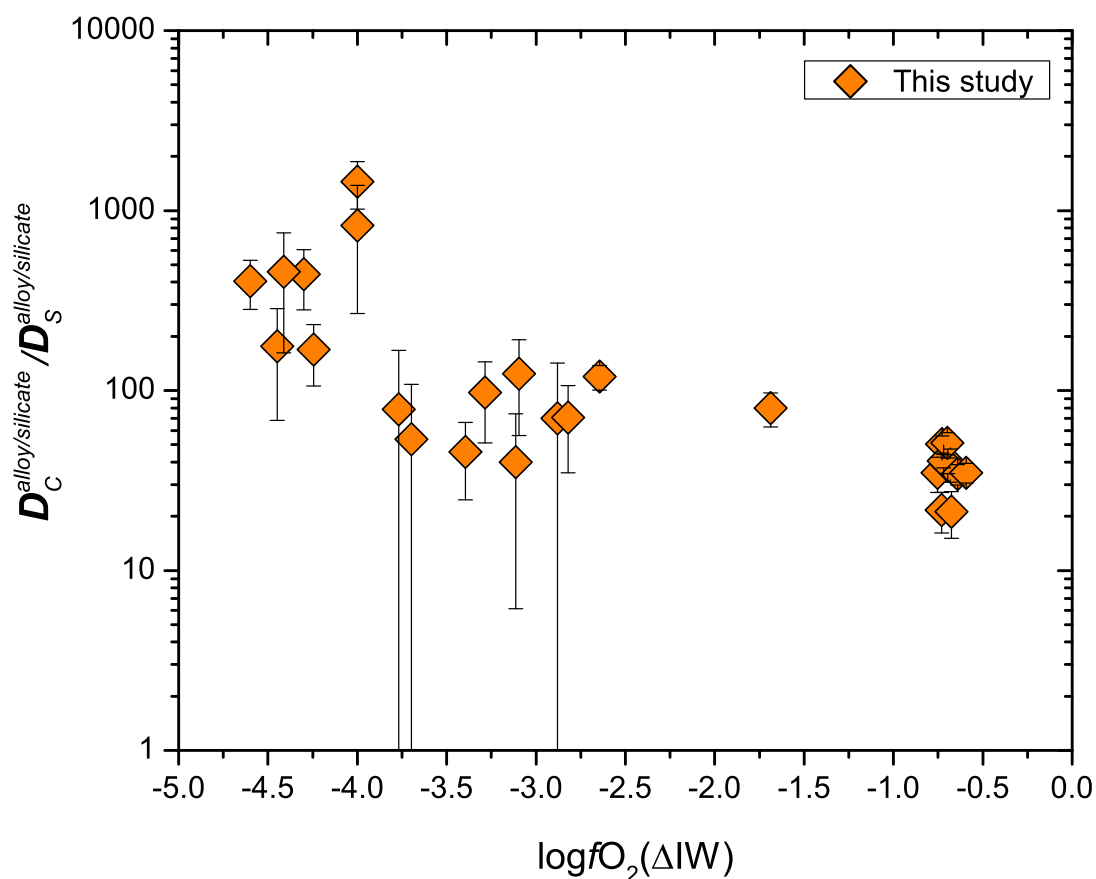


Figure S7. The $D_C^{alloy/silicate} / D_S^{alloy/silicate}$ ratio as a function of oxygen fugacity. Note that $D_C^{alloy/silicate} / D_S^{alloy/silicate}$ ratio increases from about 20 up to 1000 with oxygen fugacity decreasing from about $\Delta IW = -0.5$ to $\Delta IW = -4.5$. The data of $D_C^{alloy/silicate}$ and $D_S^{alloy/silicate}$ used in this figure are taken from the experiments in which $D_C^{alloy/silicate}$ and $D_S^{alloy/silicate}$ were simultaneously determined for the ThB/Knippha-Fe-Ni-S (<5 wt.%) \pm Si system (Table S1).

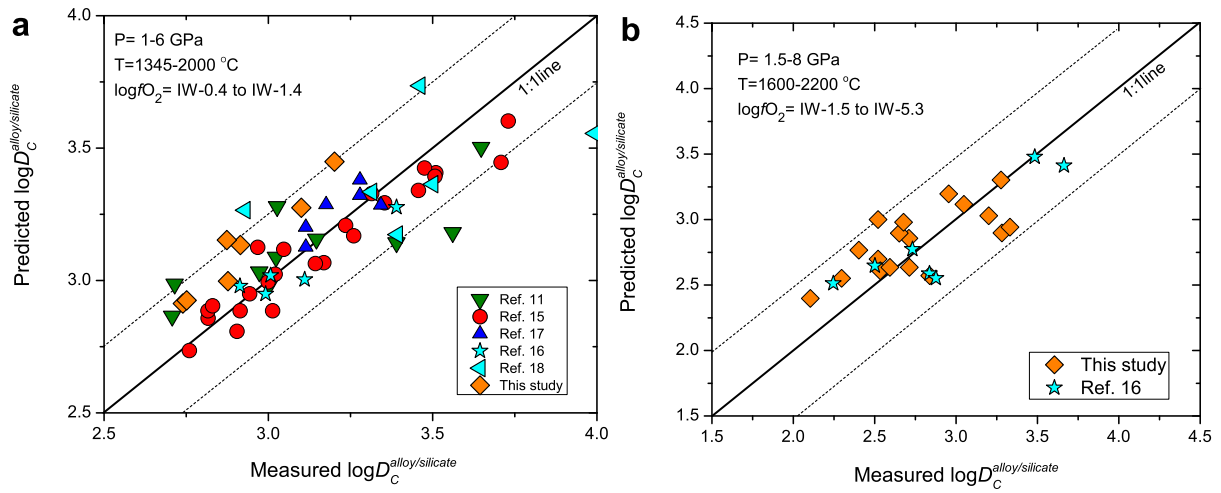


Figure S8. Comparison of the experimentally measured $\log D_C^{\text{alloy/silicate}}$ and the predicted $\log D_C^{\text{alloy/silicate}}$ using Eqs. 3-4. Note that panels (a, b) correspond to Eqs.3-4, respectively. Also note that $\log D_C^{\text{alloy/silicate}}$ can well be predicted within 0.25 log units and 0.5 log units, respectively, as indicated by the dashed lines.

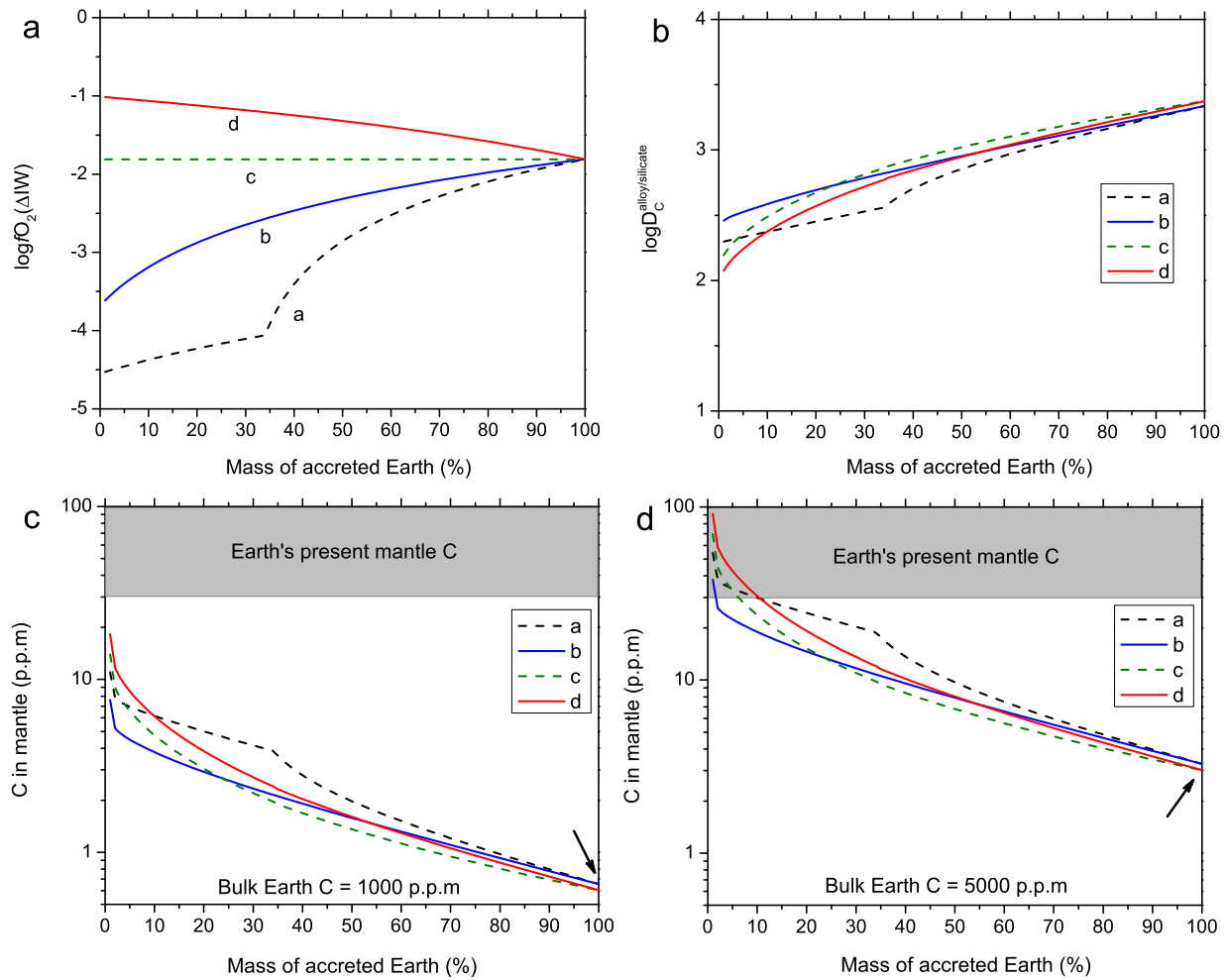


Figure S9. The possible change of oxygen fugacity, the corresponding $D_C^{alloy/silicate}$, and the calculated carbon abundance in mantle during Earth's continuous core formation. **a**, four possible variation of oxygen fugacity during Earth's accretion (ref. 3). **b**, the calculated $D_C^{alloy/silicate}$ at conditions corresponding to models a-d in panel (a), using Eqs.3-4. **c. d**, the calculated carbon abundance in Earth's mantle during continuous accretion. Note that the calculated carbon abundance in Earth's mantle (marked by the arrows in panel c and d) is significantly lower than the Earth's present mantle carbon abundance. See text for details.

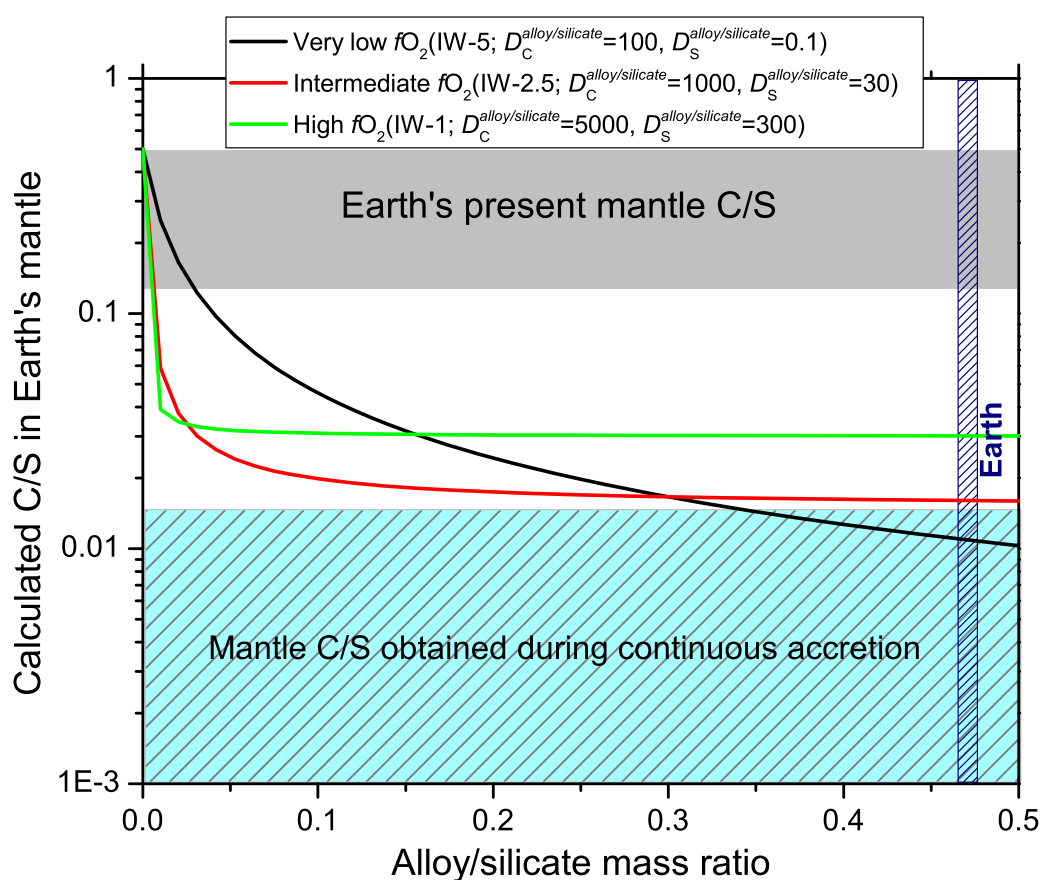


Figure S10. The calculated C/S ratio in Earth's mantle as a function of equilibrium alloy/silicate mass ratio. Three different pairs of $D_S^{\text{alloy/silicate}}$ and $D_C^{\text{alloy/silicate}}$ values were used, which correspond to very low fO_2 , intermediate fO_2 , and relatively high fO_2 MO condition. The initial C/S ratio is assumed to be 0.5, comparable to the C/S ratio in carbonaceous chondrites. The C/S ratio resulting from continuous accretion model (Supplementary Fig. 9) is plotted for comparison. C/S ratio was calculated from the mantle carbon abundance modelled in Supplementary Figure 9 and sulfur abundance modelled in ref. 3. The results show that the C/S ratio observed for Earth's present mantle cannot be produced by single stage, equilibrium core formation model with any reasonable alloy/silicate mass ratio or continuous core formation model, if carbon and sulfur were delivered simultaneously by chondritic materials during Earth's accretion. The main reason is that $D_C^{\text{alloy/silicate}}$ is exceedingly higher than $D_S^{\text{alloy/silicate}}$ and the carbon content in the silicate mantle, resulting from core-segregation, is extremely low.

Table S1. Summary of experimental conditions, products, and results.

Run No	P	T	Duration	Starting Material	Quench Products	^a logF _{O2} (ΔIW)	^b logF _{O2} (ΔIW)	Raman	¹² FIR-C	¹² FIR-OH, wt%	¹² FIR-OH, wt%	H ₂ O in silicate (SIMS)	¹³ C in silicate (SIMS)	C in alloy	D ³⁴ Sulfate	D ³⁴ Sulfate
GPa	°C	min				Ideal	Non-ideal		p.p.m	ε=50	ε=90	wt.-%	p.p.m	wt.-%	D ³⁴ Sulfate	D ³⁴ Sulfate
MA94	4	2000	7	ThB+Fe-Ni(Swt%)S (3wt%)	Glass+alloy	-1.30	-0.67	✓		0.73 ± 0.05	0.48 ± 0.03	1.1 ± 0.0	78 ± 17	5.80 ± 0.22	748 ± 170	35 ± 6
MA95	4	1800	15	ThB+Fe-Ni(Swt%)	Glass+alloy	-1.40	-0.68	✓		0.77 ± 0.05	0.51 ± 0.03	1.0 ± 0.1	48 ± 2	6.06 ± 0.41	1259 ± 94	32 ± 6
G325	3	1800	25	Knippa+ Fe-Ni(Swt%)S (3wt%)	Glass+alloy	-1.38	-0.69	✓	29 ± 2	0.26 ± 0.01	0.17 ± 0.01	0.32 ± 0.01	97 ± 6	5.49 ± 0.11	564 ± 35	15 ± 1
MA61	6	1800	20	Knippa+ Fe-Ni(Swt%)S (3wt%)	Glass+quench crystals + alloy	-1.41	-0.73	✓				0.55 ± 0.13	72 ± 14	5.95 ± 0.19	822 ± 165	38 ± 6
G324	3	1800	20	Knippa+ Fe-Ni(Swt%)S (3wt%)	Glass+alloy	-1.42	-0.73	✓	27 ± 3	0.10 ± 0.00	0.07 ± 0.00	0.14 ± 0.00	100 ± 4	5.52 ± 0.04	549 ± 22	11 ± 1
G323	3	1700	80	Knippa+ Fe-Ni(Swt%)S (3wt%)	Glass+alloy	-1.43	-0.75	✓	21 ± 1	0.15 ± 0.00	0.10 ± 0.00	0.18 ± 0.00	68 ± 0	5.15 ± 0.21	754 ± 30	22 ± 5
G388	1.5	1600	120	Knippa+ Fe-Ni(Swt%)S (7wt%)	Glass+alloy	-2.00	-1.36	✓		0.63 ± 0.01	0.42 ± 0.01	0.77 ± 0.00	31 ± 2	4.89	1589 ± 101	
G391	1.5	1600	120	Knippa+ Fe-Ni(Swt%)S (13wt%)	Glass+alloy	-2.30	-1.69	✓		0.81 ± 0.04	0.54 ± 0.03	0.81 ± 0.01	24 ± 1	5.06 ± 0.19	2141 ± 141	27 ± 5
MA84	6	2000	7	Knippa+ Fe-Ni(Swt%)S (7wt%)	Glass + alloy	-2.62	-1.92	✓		0.24 ± 0.00	0.16 ± 0.00	0.35 ± 0.00	25 ± 0	4.79 ± 0.43	1885 ± 174	
MA85	4	2000	7	Knippa+ Fe-Ni(Swt%)S (7wt%)	Glass + alloy	-2.66	-1.98	✓		0.46 ± 0.01	0.30 ± 0.01	0.56 ± 0.00	40 ± 0	4.51 ± 0.47	1117 ± 118	
G389	1.5	1600	120	Knippa+ Fe-Ni(Swt%)S (7wt%)	Glass+alloy	-3.30	-2.64	✓		0.49 ± 0.00	0.33 ± 0.00	0.66 ± 0.02	27 ± 1	5.14 ± 0.18	1910 ± 89	16 ± 2
MA77	8	2000	5	Knippa+ Fe-Ni(Swt%)S (3.5wt%)S (13wt%)	Glass + alloy	-3.54	-2.82	✓				0.27 ± 0.01	56 ± 11	5.07 ± 0.23	901 ± 175	13 ± 6
MA72	8	2200	3	Knippa+ Fe-Ni(Swt%)S (3.5wt%)S (13wt%)	Glass + alloy	-3.69	-2.88	✓				0.37 ± 0.01	99 ± 3	4.70 ± 0.29	475 ± 33	6.8 ± 7.0
MA75	4	2000	6	Knippa+ Fe-Ni(Swt%)S (3.5wt%)S (13wt%)	Glass + alloy	-3.85	-3.10	✓				0.46 ± 0.01	117 ± 56	5.23 ± 0.19	448 ± 217	3.6 ± 0.9
MA70	8	2100	5	Knippa+ Fe-Ni(Swt%)S (3.5wt%)S (13wt%)	Glass + alloy	-3.90	-3.11	✓				0.30 ± 0.04	132 ± 6	4.38 ± 0.29	332 ± 26	8.3 ± 7.0
MA73	6	2000	6	Knippa+ Fe-Ni(Swt%)S (3.5wt%)S (13wt%)	Glass + alloy	-4.04	-3.29	✓		0.25 ± 0.01	0.16 ± 0.01	0.45 ± 0.01	82 ± 3	4.23 ± 0.21	513 ± 33	5.3 ± 2.5
MA68	8	2000	6	Knippa+ Fe-Ni(Swt%)S (3.5wt%)S (13wt%)	Glass + alloy	-4.16	-3.40	✓		0.33 ± 0.01	0.22 ± 0.00	0.75 ± 0.14	195 ± 28	3.86 ± 0.27	198 ± 31	4.3 ± 1.9
MA78	8	2000	7	Knippa+ Fe-Ni(Swt%)S (3.5wt%)S (13wt%)	Glass + alloy	-4.53	-3.70	✓		0.20 ± 0.00	0.14 ± 0.00	0.69 ± 0.03	241 ± 1	3.07 ± 0.56	127 ± 23	2.4 ± 2.4
MA64	6	1800	20	Knippa+ Fe-Ni(Swt%)S (3.5wt%)S (13wt%)	Glass + alloy	-4.50	-3.77	✓		0.20 ± 0.00	0.14 ± 0.00	0.51 ± 0.01	170 ± 162	5.63 ± 1.24	331 ± 323	4.2 ± 2.4
MA66	8	1800	20	Knippa+ Fe-Ni(Swt%)S (3.5wt%)S (13wt%)	Glass + alloy	-4.70	-4.00	✓				0.24 ± 0.00	10 ± 2	4.83 ± 0.14	504 ± 1062	3.5 ± 0.7
G338	3	1800	25	Knippa+ Fe-Ni(Swt%)S (3.5wt%)S (16wt%)	Glass+quench crystals + alloy	-4.60	-4.00	✓		0.09 ± 0.00	0.06 ± 0.00	0.24 ± 0.01	146 ± 16	3.69 ± 0.46	253 ± 41	0.3 ± 0.2
G336	3	1700	60	Knippa+ Fe-Ni(Swt%)S (3.5wt%)S (16wt%)	Glass+alloy	-5.20	-4.30	✓				0.48 ± 0.00	142 ± 3	5.57 ± 0.21	392 ± 17	0.9 ± 0.3
G390	1.5	1600	120	Knippa+ Fe-Ni(Swt%)S (13wt%)	Glass+alloy	-5.20	-4.41	✓				0.24 ± 0.01	96 ± 26	3.27 ± 0.09	342 ± 92	0.7 ± 0.4
G327	3	1800	20	Knippa+ Fe-Ni(Swt%)S (15wt%)	Glass+alloy	-5.50	-4.79	✓		0.02 ± 0.00	0.02 ± 0.00	0.13 ± 0.00	56 ± 2	2.88 ± 0.31	516 ± 58	21 ± 13
G328	3	1700	60	Knippa+ Fe-Ni(Swt%)S (15wt%)	Glass+alloy	-5.99	-5.26	✓		0.02 ± 0.00	0.01 ± 0.00	0.10 ± 0.00	45 ± 1	3.12 ± 0.84	689 ± 186	
MA76	6	1800	20	Knippa+ Fe-Ni(Swt%)S (7wt%)	Fine quench crystals + alloy	-1.50	-0.83	✓								
MA79	8	2000	7	Knippa+ Fe-Ni(Swt%)S (7wt%)	Fine quench crystals + alloy	-2.85	-2.15	✓								
MA81	8	2100	3.5	Knippa+ Fe-Ni(Swt%)S (7wt%)	Fine quench crystals + alloy	-2.40	-1.68	✓								
MA83	8	2200	4	Knippa+ Fe-Ni(Swt%)S (7wt%)	Fine quench crystals + alloy	-2.27	-1.52	✓								
Partition coefficients for sulfur between metal and silicate melt are measured from the experiments published in ref.16.																
G316-02	3	1600					-0.7								1016 ± 29	25 ± 2
G315-01	3	1600					-0.6								1291 ± 86	38 ± 4
G317-03	3	1600					-0.6								981 ± 57	28 ± 3
G318-04	3	1600					-0.7								820 ± 17	16 ± 2
G330-16	3	1600					-4.2								540 ± 22	3.2 ± 1.2
G331-17	3	1600					-4.4								317 ± 8	1.8 ± 1.1
G337-19	3	1600					-4.6								176 ± 11	0.4 ± 0.1

^aIdeal f_{O_2} with respect to the Fe-FeO (IW) buffer calculated assuming ideal solution behavior of alloy and silicate melt; ^bnon-ideal f_{O_2} with respect to the Fe-FeO (IW) buffer calculated assuming non-ideal solution behavior of alloy and silicate melt.^cCarbon as carbonate.^dThe water content was measured by FTIR using the Beer-Lambert law at extinction coefficient = 60 and 90 L mol⁻¹ cm⁻¹ for water at ~3550 cm⁻¹, respectively.^ebulk water in silicate melt determined by SIMS. ^fbulk carbon in silicate melt determined by SIMS.^gmeasured; X: not measured.Glass = Silicate glass; Alloy = alloy melt; D³⁴Sulfate = -C or S in Alloy/Cor S in Glass; ThB = basalt with a MORB-like composition.

For each sample, 3-6 spots were analyzed by SIMS and 2-5 spots were analyzed by FTIR.

The Table is arranged in the order of decreasing experimental f_{O_2} except for the runs with fine quench crystals.

Table S2. Major and minor element contents and S content in silicate melts and alloy melts (in wt.%).

Run No	SiO ₂	TiO ₂	Al ₂ O ₃	Cr ₂ O ₃	FeO*	MnO	MgO	NiO	CaO	Na ₂ O	K ₂ O	P ₂ O ₅	S	Total	NBO/T	Fe	Ni	C	S	Si	Total
MA94	47.0	0.8	15.1	0.0	16.2	0.2	8.4	0.1	9.9	2.5	0.1	0.0	0.16	100.5	0.89	86.6	5.5	5.8	5.6	0.0	103.5
1-σ	0.3	0.0	0.1	0.0	0.2	0.0	0.1	0.0	0.1	0.1	0.0	0.0	0.02	0.4		0.6	0.2	0.2	0.6	0.0	0.5
MA95	46.1	0.7	14.6	0.2	16.3	0.0	8.5	0.0	9.5	2.2	0.1	0.0	0.15	98.7	0.91	86.5	6.0	6.1	4.8	0.0	103.5
1-σ	0.5	0.0	0.1	0.1	0.2	0.0	0.1	0.0	0.2	0.1	0.0	0.0	0.02	0.6		0.4	0.1	0.4	0.5	0.0	0.5
G325	38.8	3.2	10.7	0.06	17.2	0.19	12.6	0.02	11.1	2.8	1.7	0.59	0.18	99.1	1.37	89.0	5.4	5.5	2.7	0.0	102.6
1-σ	0.3	0.1	0.1	0.01	0.1	0.01	0.1	0.01	0.1	0.0	0.0	0.01	0.00	0.3		0.6	0.1	0.1	0.2	0.0	0.7
MA61	39.5	3.2	10.6	0.1	16.1	0.2	11.7	0.03	11.1	2.6	1.7	0.6	0.07	97.5	1.27	86.2	6.2	5.9	2.8	0.0	101.1
1-σ	0.4	0.0	0.1	0.0	0.5	0.0	0.4	0.01	0.2	0.1	0.1	0.1	0.01	2.0		0.5	0.4	0.2	0.3	0.0	0.4
G324	39.0	3.3	10.9	0.05	16.6	0.19	13.2	0.01	11.3	2.9	1.7	0.58	0.27	100.0	1.37	88.3	6.2	5.5	3.0	0.0	103.0
1-σ	0.2	0.1	0.1	0.01	0.2	0.01	0.1	0.01	0.1	0.1	0.0	0.01	0.01	0.4		0.6	0.2	0.0	0.3	0.0	0.5
G323	39.1	3.3	10.7	0.06	16.3	0.19	13.1	0.01	11.3	3.0	1.8	0.65	0.19	99.7	1.37	87.4	6.1	5.1	4.1	0.0	102.8
1-σ	0.1	0.2	0.1	0.01	0.2	0.01	0.2	0.01	0.1	0.1	0.0	0.01	0.01	0.3		0.8	0.1	0.2	0.9	0.0	0.4
G388	45.0	3.4	11.0	0.2	8.5	0.0	12.9	0.1	11.7	3.1	1.8	0.3	0.008	97.9	1.01	85.9	5.3	4.9	0.1	0.0	96.1
1-σ	0.7	0.1	0.1	0.0	0.1	0.0	0.1	0.0	0.1	0.1	0.0	0.1	0.009	1.0							
G391	47.2	3.4	11.1	0.2	6.0	0.0	13.3	0.1	12.0	3.2	1.8	0.22	0.08	98.6	0.93	88.0	5.4	5.1	2.3	0.0	100.7
1-σ	0.9	0.1	0.1	0.0	0.2	0.0	0.1	0.0	0.3	0.1	0.1	0.05	0.01	1.2		0.4	0.1	0.2	0.3	0.0	0.4
MA84	49.2	0.3	11.3	0.0	4.5	0.0	13.0	0.01	12.2	2.9	1.8	0.1	0.0	95.3	1.05	89.9	5.0	4.8	0.01	0.04	99.7
1-σ	0.2	0.0	0.1	0.0	0.1	0.0	0.1	0.01	0.1	0.1	0.1	0.1	0.0	0.9		0.6	0.4	0.4	0.0	0.0	0.4
MA85	45.9	3.3	10.4	0.0	4.4	0.2	17.2	0.02	11.3	2.6	1.7	0.0	0.0	97.0	1.11	89.9	5.0	4.5	0.0	0.1	99.5
1-σ	0.4	0.0	0.1	0.0	0.1	0.0	0.5	0.01	0.1	0.1	0.1	0.0	0.0	1.5		0.7	0.3	0.5	0.0	0.0	0.8
G389	49.8	3.6	11.2	0.2	1.8	0.0	13.7	0.0	12.1	3.3	1.8	0.0	0.28	98.1	0.81	87.7	5.1	5.1	4.4	0.0	102.4
1-σ	0.5	0.1	0.2	0.0	0.1	0.0	0.2	0.0	0.1	0.1	0.1	0.0	0.03	0.7		0.5	0.1	0.2	0.5	0.0	0.4
MA77	54.4	3.4	11.4	0.0	1.5	0.1	13.0	0.01	12.3	2.9	1.8	0.0	0.2	101.4	0.72	86.5	5.1	5.1	2.5	0.8	100.0
1-σ	0.3	0.0	0.1	0.0	0.2	0.0	0.2	0.01	0.2	0.1	0.1	0.0	0.01	1.3		1.2	0.2	0.2	1.2	0.0	0.5
MA72	53.3	3.0	11.0	0.0	1.2	0.1	13.0	0.01	12.0	2.8	1.9	0.0	0.5	99.2	0.75	84.2	4.9	4.7	3.1	3.2	100.1
1-σ	0.8	0.0	0.2	0.0	0.5	0.0	0.3	0.01	0.1	0.1	0.0	0.0	0.1	2.4		3.1	0.5	0.3	3.0	0.4	1.2
MA75	55.1	3.1	11.0	0.0	1.0	0.1	13.2	0.0	11.8	2.4	1.8	0.0	0.7	100.8	0.71	84.5	5.0	5.2	2.4	2.5	99.6
1-σ	0.2	0.0	0.1	0.0	0.3	0.0	0.2	0.0	0.1	0.1	0.1	0.0	0.0	1.2		1.9	0.2	0.2	0.6	0.1	1.9
MA70	53.3	3.1	11.0	0.0	0.9	0.1	13.2	0.01	12.0	3.1	1.8	0.0	0.4	99.5	0.76	83.3	4.6	4.4	3.5	3.2	99.0
1-σ	0.2	0.0	0.1	0.0	0.1	0.0	0.2	0.00	0.1	0.1	0.1	0.0	0.0	1.0		3.3	0.4	0.3	3.0	0.3	1.3
MA73	56.1	3.0	11.7	0.0	0.8	0.1	12.7	0.01	12.1	2.7	1.8	0.0	0.5	102.2	0.68	83.7	4.8	4.2	2.8	2.8	98.3
1-σ	0.6	0.1	0.1	0.0	0.1	0.0	0.2	0.01	0.1	0.2	0.1	0.0	0.0	1.5		2.6	0.3	0.2	1.3	0.2	2.1
MA68	54.9	3.0	11.4	0.0	0.7	0.1	13.4	0.02	12.2	3.0	1.8	0.0	0.5	101.6	0.73	83.7	5.2	3.9	2.2	3.2	98.2
1-σ	0.6	0.0	0.1	0.0	0.1	0.0	0.3	0.01	0.1	0.2	0.1	0.0	0.0	1.6		2.0	0.2	0.3	1.0	0.2	1.9
MA78	55.1	2.8	11.3	0.0	0.5	0.1	13.3	0.01	12.1	3.0	1.8	0.1	0.7	101.4	0.73	82.4	5.4	3.1	1.7	6.5	99.2
1-σ	0.9	0.0	0.2	0.0	0.1	0.0	0.5	0.02	0.1	0.2	0.1	0.0	0.0	2.2		2.2	0.3	0.6	1.8	0.3	1.6
MA64	54.0	3.1	11.2	0.0	0.5	0.1	13.1	0.0	12.0	2.9	1.9	0.0	0.6	99.9	0.72	82.9	5.0	5.6	2.4	3.0	98.9
1-σ	0.8	0.0	0.2	0.0	0.1	0.0	0.4	0.0	0.1	0.2	0.0	0.0	0.0	1.9		3.0	0.3	1.2	1.3	0.2	1.2
MA66	54.4	3.0	11.5	0.0	0.4	0.1	13.1	n.d	12.0	3.0	1.9	0.0	0.4	99.94	0.86	85.1	5.5	4.8	1.2	3.3	100.0
1-σ	0.3	0.1	0.2	0.0	0.1	0.0	0.4		0.3	0.2	0.3	0.0	0.1	0.57		0.1	0.0	0.1	0.1	0.0	0.0
G338	54.7	3.0	11.8	0.01	0.4	0.11	14.1	0.01	11.8	2.8	1.8	0.00	2.0	102.53	0.74	85.1	5.5	3.7	0.6	6.1	101.0
1-σ	0.4	0.2	0.1	0.01	0.1	0.01	0.1	0.00	0.1	0.1	0.0	0.00	0.0	0.58		1.8	0.2	0.5	0.4	0.2	1.4
G336	53.7	3.3	11.7	0.01	0.3	0.14	13.7	0.00	11.8	3.0	1.9	0.00	1.7	101.26	0.72	86.2	5.2	5.6	1.5	3.0	101.5
1-σ	0.7	0.1	0.1	0.00	0.0	0.01	0.1	0.01	0.1	0.1	0.0	0.00	0.0	0.93		1.5	0.1	0.2	0.6	0.1	1.6
G390	55.4	2.3	10.6	0.1	0.2	0.0	12.8	0.0	11.5	2.9	1.7	0.0	3.33	103.1	0.73	82.2	5.6	3.3	2.5	7.8	101.4
1-σ	0.6	0.1	0.2	0.0	0.1	0.0	0.1	0.0	0.3	0.1	0.1	0.0	0.08	0.7		1.6	0.2	0.1	1.5	0.3	0.9
G327	54.1	2.7	11.9	0.00	0.2	0.09	14.0	0.00	12.6	3.1	2.0	0.00	0.00	100.5	0.78	85.7	5.4	2.9	0.0	7.8	101.8
1-σ	0.3	0.1	0.1	0.00	0.0	0.01	0.1	0.00	0.1	0.1	0.0	0.01	0.00	0.4		0.5	0.1	0.3	0.0	0.2	0.5
G328	54.4	2.8	12.2	0.00	0.1	0.09	14.4	0.00	12.5	2.9	2.0	0.00	0.00	101.1	0.77	83.8	5.1	3.1	0.0	7.7	100.4
1-σ	0.3	0.1	0.1	0.00	0.0	0.01	0.1	0.00	0.1	0.0	0.0	0.00	0.00	0.4		3.9	0.3	0.8	0.0	0.4	2.3
MA76	40.0	3.3	10.8	0.1	14.8	0.2	12.2	0.03	11.5	2.3	1.6	0.5	0.15	97.5	1.23	86.9	5.3	5.4	3.2	0.0	100.8
1-σ	0.4	0.1	0.2	0.0	0.8	0.0	0.6	0.03	0.3	0.7	0.4	0.1	0.04	3.8		1.3	0.7	0.2	1.8	0.0	0.2
MA79	47.8	3.4	11.1	0.0	3.5	0.2	15.2	0.01	13.4	2.6	1.5	0.1	0.0	98.8	0.99	90.5	4.2	5.5	0.0	0.0	100.1
1-σ	0.3	0.5	0.2	0.0	0.3	0.0	0.3	0.01	0.3	0.1	0.1	0.0	0.0	2.1		0.4	0.4	0.5	0.0	0.0	0.5
MA81	46.6	3.1	10.6	0.0	5.9	0.2	15.5	0.02	12.8	2.4	1.7	0.1	0.0	98.9	1.10	88.9	5.0	5.6	0.0	0.0	99.5
1-σ	0.3	0.2	0.1	0.0	0.4	0.0	0.2	0.01	0.2	0.2	0.1	0.0	0.0	1.8		0.6	0.1	0.3	0.0	0.0	0.4
MA83	47.1	3.3	10.8	0.0	6.8	0.2	13.3	0.03	12.6	2.3	1.5	0.1	0.0	98.1	0.97	89.5	4.9	4.9	0.0	0.0	99.3
1-σ	0.9	0.1	0.1	0.0	0.2	0.0	0.5	0.02	0.2	0.1	0.1	0.0	0.0	2.3		1.3	0.6	0.4	0.0	0.0	1.1

NBO/T = 2 total O/T - 4 (T = Si + Ti + Al + Cr + P). For each sample, typically 10-20 spots were analyzed, and 1-σ is the standard deviation based on the replicate analyses.

Only one experiment, G388, had one spot analysis on the alloy melt pool and hence no compositional error could be calculated for that phase.

FeO* indicates total Fe.

References:

1. Wood, B. J., Walter, M. J. & Wade, J. Accretion of the Earth and segregation of its core. *Nature* **441**, 825-833 (2006).
2. Rubie, D., Melosh, H., Reid, J., Liebske, C. & Richter, K. Mechanisms of metal–silicate equilibration in the terrestrial magma ocean. *Earth Planet. Sci. Lett.* **205**, 239-255 (2003).
3. Boujibar, A. *et al.* Metal–silicate partitioning of sulphur, new experimental and thermodynamic constraints on planetary accretion. *Earth Planet. Sci. Lett.* **391**, 42-54 (2014).
4. Litasov, K. & Ohtani, E. Phase relations and melt compositions in CMAS–pyrolite–H₂O system up to 25 GPa. *Phys. Earth Planet. Inter.* **134**, 105-127 (2002).
5. Andraut, D. *et al.* Solidus and liquidus profiles of chondritic mantle: Implication for melting of the Earth across its history. *Earth Planet. Sci. Lett.* **304**, 251-259 (2011).
6. Marty, B. The origins and concentrations of water, carbon, nitrogen and noble gases on Earth. *Earth Planet. Sci. Lett.* **313**, 56-66 (2012).
7. Rosenthal, A., Hauri, E. & Hirschmann, M. Experimental determination of C, F, and H partitioning between mantle minerals and carbonated basalt, CO₂/Ba and CO₂/Nb systematics of partial melting, and the CO₂ contents of basaltic source regions. *Earth Planet. Sci. Lett.* **412**, 77-87 (2015).
8. Wang, Z. & Becker, H. Ratios of S, Se and Te in the silicate Earth require a volatile-rich late veneer. *Nature* **499**, 328-331 (2013).
9. McDonough, W. F. & Sun, S.-S. The composition of the Earth. *Chem. Geol.* **120**, 223-253 (1995).
10. Bergin, E. A., Blake, G. A., Ciesla, F., Hirschmann, M. M. & Li, J. Tracing the ingredients for a habitable earth from interstellar space through planet formation. *Proc. Natl. Acad. Sci.* **112**, 8965-8970 (2015).
11. Dasgupta, R., Chi, H., Shimizu, N., Buono, A. S. & Walker, D. Carbon solution and partitioning between metallic and silicate melts in a shallow magma ocean: implications for the origin and distribution of terrestrial carbon. *Geochim. Cosmochim. Acta* **102**, 191-212 (2013).

-
12. Hirschmann, M. M. Constraints on the early delivery and fractionation of Earth's major volatiles from C/H, C/N, and C/S ratios. *Am. Mineral.* **101**, 540-553 (2016).
 13. Li, Y., Marty, B., Shcheka, S., Zimmermann, L. & Keppler, H. Nitrogen isotope fractionation during terrestrial core-mantle separation. *Geochem. Persp. Lett.* **2**, 138-147 (2016).
 14. Wasson, J. T. & Kallemeyn, G. W. Compositions of Chondrites. *Philosophical Transactions of the Royal Society of London A: Mathematical, Physical and Engineering Sciences* **325**, 535-544 (1988).
 15. Chi, H., Dasgupta, R., Duncan, M. S. & Shimizu, N. Partitioning of carbon between Fe-rich alloy melt and silicate melt in a magma ocean—Implications for the abundance and origin of volatiles in Earth, Mars, and the Moon. *Geochim. Cosmochim. Acta* **139**, 447-471 (2014).
 16. Li, Y., Dasgupta, R. & Tsuno, K. The effects of sulfur, silicon, water, and oxygen fugacity on carbon solubility and partitioning in Fe-rich alloy and silicate melt systems at 3 GPa and 1600 °C: Implications for core–mantle differentiation and degassing of magma oceans and reduced planetary mantles. *Earth Planet. Sci. Lett.* **415**, 54-66 (2015).
 17. Stanley, B. D., Hirschmann, M. M. & Withers, A. C. Solubility of C-O-H volatiles in graphite-saturated martian basalts. *Geochim. Cosmochim. Acta* **129**, 54-76 (2014).
 18. Armstrong, L. S., Hirschmann, M. M., Stanley, B. D., Falksen, E. G. & Jacobsen, S. D. Speciation and solubility of reduced C–O–H–N volatiles in mafic melt: Implications for volcanism, atmospheric evolution, and deep volatile cycles in the terrestrial planets. *Geochim. Cosmochim. Acta* **171**, 283-302 (2015).